crystals

MDPI

Article

Phase-Field Simulation of the Creep Mechanism in the AZ31 Magnesium Alloy Under Discontinuous Dynamic Recrystallization Dominance

Alireza Rezvani [1], Ramin Ebrahimi [1,*] and Ebad Bagherpour [2,*]

[1] Department of Materials Science and Engineering, School of Engineering, Shiraz University, Shiraz 7134851154, Iran; a.rezvani@shirazu.ac.ir
[2] Brunel Centre for Advanced Solidification Technology (BCAST), Brunel University of London, Uxbridge UB8 3PH, UK
* Correspondence: ebrahimy@shirazu.ac.ir (R.E.); ebad.bagherpour@brunel.ac.uk (E.B.)

Abstract: Discontinuous dynamic recrystallization is a critical microstructural evolution mechanism during high-temperature deformation, influencing material properties significantly. This study develops a two-dimensional phase-field model to predict steady-state creep rates in the AZ31 magnesium alloy, focusing on DRX during creep. To enhance simulation accuracy, initial microstructures are generated from optical microscopy data, enabling simulations at larger scales with higher representativeness. A novel nucleation methodology is implemented, eliminating the need for nuclei order parameter adaptation, improving computational efficiency. Finite element analysis (FEA) is integrated to capture initial instantaneous deformation. The Kocks–Mecking model is employed to describe the evolution of average dislocation density, accounting for work hardening and dynamic recovery within the initial polycrystalline microstructure. Instead of conventional creep testing, impression creep, a cost-effective alternative, is used for validation. This method provides constant stress and steady penetration velocity, simulating creep conditions effectively. The model accurately predicts recrystallization kinetics and microstructural evolution, exhibiting a strong correlation with experimental results, with an error of approximately 5%. This research provides a robust and efficient approach for predicting creep behavior in high-temperature applications, vital for optimizing material selection and predicting component lifespan in industries. The methodology offers a significant advancement in understanding and predicting DRX-driven creep behavior.

Keywords: impression creep; phase-field; dynamic recrystallization; magnesium alloy AZ31; microstructural evolution

Academic Editor: Benilde F. O. Costa

Received: 15 April 2025
Revised: 6 May 2025
Accepted: 8 May 2025
Published: 12 May 2025

Citation: Rezvani, A.; Ebrahimi, R.; Bagherpour, E. Phase-Field Simulation of the Creep Mechanism in the AZ31 Magnesium Alloy Under Discontinuous Dynamic Recrystallization Dominance. *Crystals* **2025**, *15*, 453. https://doi.org/10.3390/cryst15050453

1. Introduction

Dynamic recrystallization (DRX) [1,2], meta-dynamic recrystallization (MDRX) [3–5], and static recrystallization (SRX) [6–8] are the primary mechanisms of microstructural evolution in metals and alloys. Among them, DRX occurs during plastic deformation at elevated temperatures, where the formation of new, strain-free grains replaces the deformed microstructure. However, it is important to note that DRX does not occur in all materials; it is particularly prevalent in materials with low-to-medium stacking fault energies [9]. This process is driven by the accumulation of dislocations and the resulting stored energy, which promotes the nucleation and growth of new grains. DRX is particularly significant in hot working processes, such as rolling, forging, and extrusion, as it helps to refine the

grain structure, enhance mechanical properties, and reduce flow stress [10]. Consequently, the elucidation of grain structure evolution during dynamic recrystallization (DRX) is paramount for the rational design of thermomechanical processing regimes, enabling the attainment of targeted microstructural morphologies and the subsequent modulation of alloy material properties. To this end, predictive models have been formulated to describe microstructural transformations and DRX kinetics. These include, but are not limited to, the Johnson–Mehl–Avrami–Kolmogrov (JMAK) phenomenological model [9] and physically based models that employ internal state variables such as dislocation density and subgrain size to characterize DRX evolution [11,12]. The advancement of computational resources has enhanced the adoption of microstructure-based simulation methodologies. Peczak et al. [13] and Rollett et al. [14] utilized the Monte Carlo (MC) method to simulate various aspects of dynamic recrystallization (DRX) during thermomechanical deformation. Goetz et al. [15] employed a cellular automaton (CA) approach to model DRX, noting its capacity for calibration to spatial and temporal scales, a feature distinct from the MC method. Ding et al. [16] developed a cellular automaton (CA) model, integrating microstructural evolution with plastic flow behavior and establishing a correlation between microstructural properties and the Zener–Hollomon parameter. This model has demonstrated broad applicability across diverse materials and phenomena, including magnesium alloys [17–19]. Phase-field (PF) models have emerged as a powerful tool for investigating microstructural evolution during recrystallization across diverse materials and deformation conditions. Notably, PF models offer an advantage over cellular automaton (CA) and Monte Carlo (MC) methods by inherently incorporating interfacial energy and curvature, enabling a more accurate representation of complex microstructural morphologies. These PF models, encompassing both static and dynamic recrystallization (SRX and DRX), have integrated various physical mechanisms and demonstrated broad applicability across a wide range of materials [20–26]. Takaki et al. [27,28] developed a PF model of DRX and extended the model by replacing the flow-stress model with an elastic–plastic finite element model in polycrystalline copper [28]. Similar models were developed by Zhao et al. [29,30] and Chen et al. [31].

Dynamic recrystallization (DRX) also plays a critical role in influencing the mechanical behavior of materials during high-temperature deformation. It induces significant softening of the crystalline structure, which is manifested by a pronounced stress drop in stress–strain curves and a corresponding increase in creep rate observed in creep curves [32].

The extent of this phenomenon is governed by the kinetics of DRX and the resulting microstructure, which determine the rate at which the recrystallized state is achieved. The increase in creep rate is particularly dependent on the interplay between the initial microstructure and the evolution of the recrystallized grains, as well as the rate at which new, strain-free grains form and grow under applied stress. Thus, the creep behavior is intrinsically linked to the dynamics of DRX, underscoring the importance of recrystallization kinetics in controlling the mechanical response of materials under high-temperature deformation conditions [33,34].

Creep and hot deformation are two high-temperature deformation processes that differ primarily in their loading conditions and experimental approaches. In creep, a constant external stress is applied to the material, and the resulting strain is measured as a function of time, reflecting the material's time-dependent deformation behavior. In contrast, hot deformation involves imposing a constant strain rate on the material, and the corresponding stress response is observed. This distinction in loading conditions—constant stress in creep versus constant strain rate in hot deformation—leads to different macroscopic mechanical responses and testing methodologies. However, at the microscopic scale, both processes share fundamental similarities in terms of dislocation activity and

plastic deformation mechanisms. Thus, while the macroscopic loading conditions differ, the underlying microscopic mechanisms of plastic deformation are essentially the same [35].

Given the similarities in the underlying microscopic mechanisms of plastic deformation between creep and hot deformation, the models developed to predict discontinuous dynamic recrystallization (DDRX) in hot deformation can also be applied to the DDRX process occurring during creep. However, certain modifications are necessary to account for the specific loading conditions and time-dependent nature of creep. For instance, the strain rate in creep is not constant but evolves over time to a steady-state condition. Therefore, while the core principles of DDRX models remain valid, adjustments must be made to incorporate the unique aspects of creep. By adapting these models, it becomes possible to accurately predict DDRX behavior in creep, leveraging the established framework of hot deformation while addressing the distinct characteristics of creep deformation.

The primary objective of this investigation is to develop a two-dimensional phase-field model for the prediction of the steady-state creep rate in the AZ31 magnesium alloy, achieved through the simulation of microstructural evolution during discontinuous dynamic recrystallization (DDRX). To enhance the representativeness of the simulations, initial microstructures are generated from optical microscopy data, rather than relying on synthetic or limited-scale electron backscatter diffraction (EBSD) datasets. This approach facilitates larger-scale simulations, more closely approximating industrial processing conditions, while maintaining cost-effectiveness and accessibility. Furthermore, a novel and efficient nucleation methodology is implemented, eliminating the holding time required for nuclei order parameter adaptation within the system. Additionally, finite element analysis (FEA) is integrated to determine the initial instantaneous deformation. The phase-field model of discontinuous dynamic recrystallization (PF-DDRX) incorporates the Kocks–Mecking (KM) model [36,37] to describe the evolution of average dislocation density, accounting for work hardening and dynamic recovery (DRV) within the initial polycrystalline microstructure. Creep deformation is simulated by adjusting the finite difference grid size, maintaining a constant simulation area.

However, instead of the expensive conventional creep testing, the impression creep technique is used. Impression creep is a small specimen testing technique that has been employed for many years as an alternative to the costly and time-consuming conventional uniaxial tensile creep test. It is a modified indentation test wherein the conical or ball indenter is replaced by a cylindrical flat-bottomed one. This replacement provides constant stress and steady penetration velocity at a constant load [38,39].

Magnesium alloys, including AZ31, exhibit considerable potential for lightweighting applications in the automotive and aerospace sectors due to their superior specific strength and stiffness [40]. However, a critical engineering bottleneck hindering their wider adoption, particularly in high-temperature environments such as automotive powertrain components and certain aerospace structures, is their inherent limitation in creep resistance [41,42]. Overcoming this limitation necessitates accurate prediction of the steady-state creep rate, which is paramount for the design and long-term performance assessment of high-temperature structural components in numerous industrial applications, including power generation, aerospace, and chemical processing. In these environments, materials are subjected to sustained loads and elevated temperatures, leading to time-dependent deformation that can ultimately result in component failure. Precise creep rate prediction allows engineers to optimize material selection, establish safe operating limits, and predict component lifespan, thereby ensuring structural integrity, preventing catastrophic failures, and minimizing costly downtime. Reliable creep rate estimations are therefore essential for the development of robust and efficient high-temperature systems [43].

To validate the predictive capabilities of the developed model, impression creep tests were conducted at varying impression depths, accompanied by microscopic characterization of the resulting microstructures. Comparative analysis of experimental and simulated results demonstrated a strong correlation, thereby substantiating the model's robustness in accurately predicting recrystallization kinetics and microstructural evolution.

2. Experimental Procedure

2.1. Microstructural Characterization

The material employed in this study is a commercial AZ31 magnesium alloy with a chemical composition determined by quantometric analysis and presented in Table 1.

Table 1. Chemical composition of the AZ31 magnesium alloy used in this study (wt. (%)).

Al	Zn	Mn	Si	Cu	Fe	Be	Mg
3.11	1.02	0.18	0.07	0.012	0.019	0.0008	Bal.

To establish a stable initial microstructure for subsequent creep testing, the as-received material was homogenized at 450 °C for 5 h and then furnace-cooled. The homogenized microstructure of the AZ31 alloy is depicted in Figure 1a. Microstructural analysis was performed using optical microscopy after mechanical polishing and chemical etching with an acetic picral solution (5 g picric acid, 5 mL acetic acid, 10 mL distilled water, and 100 mL ethyl alcohol). A fully homogenized microstructure, comprising 91 grains with a mean size of 32.4 µm, was observed. This characterization was achieved through a custom MATLAB R2023a script, which performed binary image conversion and subsequent analysis, including grain identification, indexing, and size determination. The resulting indexed and color-coded grain map and grain size distribution are illustrated in Figures 1b and 1c, respectively.

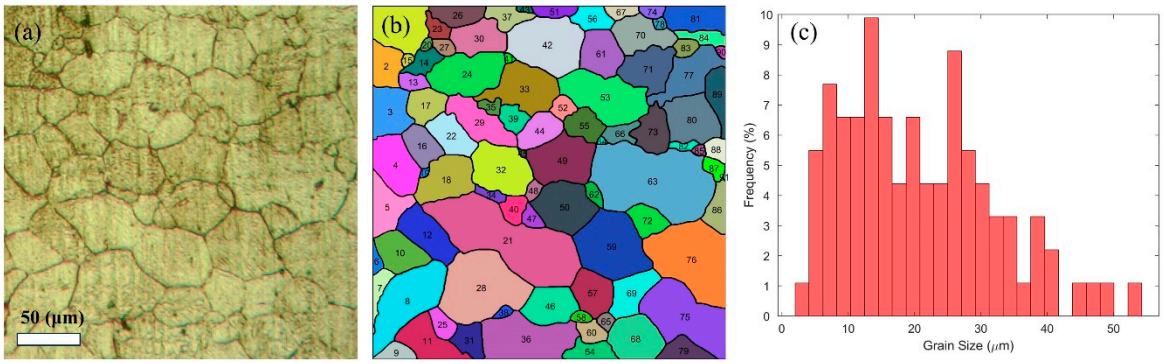

Figure 1. (**a**) Microstructure of the as-homogenized AZ31 Mg alloy. (**b**) Digitized and indexed matrix. (**c**) Grain size distribution.

2.2. Impression Creep Testing

The impression creep testing apparatus utilized in this study is comprehensively detailed in prior research [44]. The system is an in-house designed testing machine, functionally analogous to those reported by Zhang et al. [45] and Kim [46]. It is equipped with a flat-bottomed cylindrical tungsten carbide indenter, measuring 2 mm in diameter. Specimens with dimensions of 15 mm × 15 mm × 10 mm were prepared from the previously homogenized material using wire-cut electrical discharge machining (EDM).

The experimental procedure for the impression creep tests is depicted in Figure 2. During the tests, the specimens were initially heated to a temperature of 250 °C at a rate of

0.6 K/s. Subsequently, an isothermal dwell period of 300 s was implemented to ensure thermal homogeneity and minimize temperature gradients within the specimens. Following the stabilization period, a constant stress of 200 MPa was applied. Upon completion of the creep test, specimens were rapidly quenched in a water bath. Throughout the experimental procedure, the temperature was maintained within a tolerance of ±1 °C of the target value, ensuring precise thermal control.

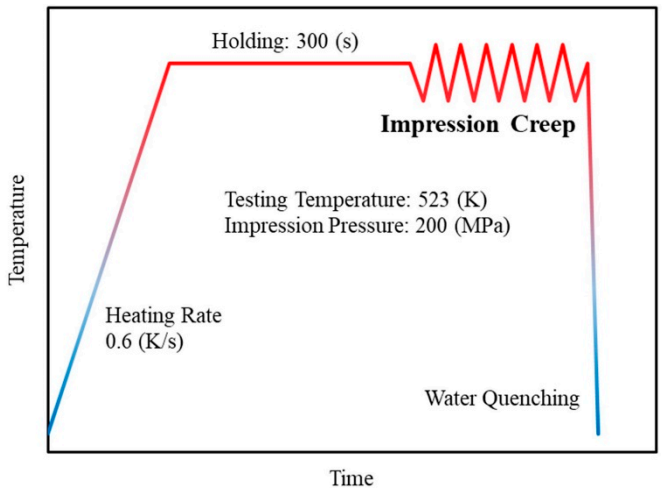

Figure 2. The experimental scheme of the impression creep test.

To elucidate the discontinuous dynamic recrystallization (DDRX) mechanisms operative during impression creep, microstructural analysis was focused on the region directly beneath the center of the indenter. This zone, characterized by unidirectional downward material flow [44,47,48], represents the preferential nucleation site for DDRX. For microstructural characterization, deformed specimens were sectioned axially, bisecting the impression cavity (as depicted in Figure 3). The sectioned surfaces were then prepared using standard metallographic techniques, including sequential grinding and polishing, suitable for optical microscopy.

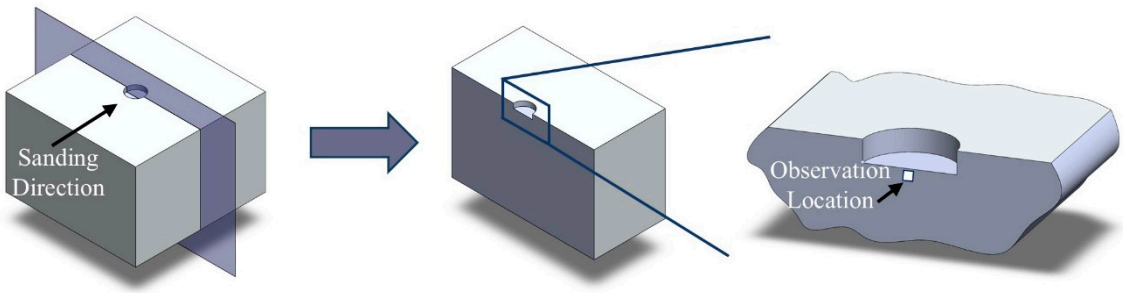

Figure 3. Schematic representation of the specimen preparation process, highlighting the axial cross-section of the impression hole for microstructural analysis.

2.3. Finite Element Analysis

The impression creep test has been subjected to extensive scrutiny via finite element analysis (FEA) in prior research [47,49,50]. While a comprehensive FEA approach has been established within the existing literature, this current investigation will utilize FEA solely for the determination of the instantaneous impression depth resulting from the initial application of a constant load to the indenter. The focus is limited to the elastic–plastic response immediately following loading, rather than the time-dependent creep deformation evolution.

The axisymmetric geometric model of the specimen, along with the rigid indenter, was imported into the Deform-3D ver. 11.0 simulation environment. The indenter was designed with a 0.1 mm (5% of the indenter diameter) fillet to avoid stress concentration at the edges [50]. Material properties, including temperature-dependent flow stress data obtained from Liu et al. [51], were incorporated into the model using a custom key to ensure consistency in all material properties used in this study. Boundary conditions were applied to replicate the experimental setup, including fixed supports, applied force on the indenter, and thermal boundary conditions. Friction at the contact interfaces was modeled using a shear friction model with a coefficient of 0.35 [44]. The simulation parameters, such as time step size and remeshing criteria, were optimized to ensure numerical stability.

3. Multi-Phase-Field DDRX Model

To investigate grain structure evolution during discontinuous dynamic recrystallization (DDRX) under deformation, a phase-field model with multi-order parameters was utilized. The model's total free energy, representing the inhomogeneous system, is a functional of the orientation field and its gradients. It includes contributions from bulk free energy (F_{bulk}), interfacial free energy (F_{int}) [52], and stored energy field (F_s) due to plastic deformation from dislocation generation [21,23]. This total free energy is defined as follows:

$$\mathcal{F} = F_{bulk} + F_{int} + F_s = \int_V \left[f_{bulk}(\{\eta_i\}) + f_{int}(\{\eta_i\}, \{\nabla\eta_i\}) + f_s(\{\eta_i\}) \right] dV \tag{1}$$

where V is the volume of the system and η_i denotes the orientation field variables, also known as order parameters [53], used to differentiate individual grains. Two distinct sets of order parameters are employed: $\eta_{i_{DEF}}$ $(i = 1, \ldots, g_d)$ to describe the initial grains that deform during the simulation and $\eta_{i_{DRX}}$ $(i = 1, \ldots, g_n)$ to represent the DRX nuclei. g_d denotes the total number of grains before discontinuous dynamic recrystallization, while g_n represents the number of DDRX nuclei, which increases as the nucleation process proceeds.

The bulk energy term establishes uniform potential wells within grain interiors, driving grain growth and the subsequent filling of the simulation domain. Conversely, the gradient energy density is localized to grain boundary regions [54]. These energy contributions are mathematically represented as follows:

$$f_{bulk} + f_{int} = m_0 \left[\sum_{i=1}^{g} \left(\frac{\eta_i^4}{4} - \frac{\eta_i^2}{2} \right) + \gamma \sum_{i=1}^{g} \sum_{j>i}^{g} \eta_i^2 \eta_j^2 + \frac{1}{4} \right] + \frac{\kappa}{2} \sum_{i=1}^{g} |\nabla\eta_i|^2 \tag{2}$$

where g is the total number of order parameters, m_0 is the energy density coefficient, and γ is a positive constant set to 1.5 for symmetrical order parameter values across the grain boundaries. The gradient energy penalty, κ, affects both the grain boundary energy and thickness [55].

The driving force for DRX nuclei growth, arising from the high dislocation density in deformed grains, is provided by the stored plastic deformation energy density term. This term is approximated by the stress field of dislocations generated during plastic deformation, as follows [56]:

$$f_S = \frac{1}{2} \rho G b^2 \tag{3}$$

where b is the magnitude of the burgers vector and G is the shear modulus. The dislocation density field, ρ, is determined at each point from the order parameters and their respective dislocation densities [22] through the application of Moelans' interpolation function [57,58]:

$$\rho(\eta_1, \eta_2, \ldots, \eta_g) = \frac{\sum_{i=1}^{g} \eta_i^2 \rho_g}{\sum_{j=1}^{g} \eta_j^2} \tag{4}$$

The dislocation density at each grid point, ρ_g, is obtained from the dislocation evolution inside the microstructure during the plastic deformation process.

The microstructural evolution is governed by the time-dependent Ginzburg–Landau equation [53], also referred to as the Allen–Cahn equation [59], which is formulated using a non-conserved order parameter:

$$\frac{\partial \eta_i(r,t)}{\partial t} = -L\frac{\delta \mathcal{F}}{\delta \eta_i(r,t)} \tag{5}$$

where L is the relaxation coefficient related to the interfacial mobility, t is time, and r is the spatial position of order parameters in the system. Utilizing the total free energy function, as defined in Equation (1), the evolution equation governing the system's behavior is expressed as follows [22]:

$$\frac{\partial \eta_i}{\partial t} = -L\left[m_0\left(-\eta_i + \eta_i^3 + 2\gamma\eta_i\sum_{j\neq i}^{g}\eta_j^2\right) - \kappa\nabla^2\eta_i + Gb^2\frac{\eta_i}{\sum_{j=1}^{g}\eta_j^2}\left(\rho_g - \rho\right)\right] \quad \begin{matrix} i \\ = 1,2,\ldots,g \end{matrix} \tag{6}$$

The spatiotemporal evolution of the dynamic microstructure is determined by numerically solving Equation (6), coupled with constitutive equations describing dislocation evolution and discontinuous dynamic recrystallization nucleation. A finite difference method is employed to obtain numerical solutions to this coupled system of kinetic equations. This method discretizes the continuous system onto a discrete lattice [53]. The phase-field equations are similarly discretized, yielding a system of algebraic equations. The solution to these algebraic equations provides the phase-field variables at each lattice node. A common and computationally efficient approach utilizes a finite difference discretization with uniform lattice spacing, employing a central second-order spatial discretization and a forward Euler temporal discretization.

To reduce computational cost and resource consumption, active parameter tracking [60,61] is employed. The computational complexity arising from the numerous DRX nuclei within the system necessitates an efficient approach. To address this, a sparse data structure is implemented, exploiting the localized activity of phase-field variables. By restricting computations to the non-zero order parameters at each grid point, a significant reduction in computational effort is achieved. The determination of the active order parameters at each location is defined as follows:

$$\mathcal{P}(r,t) = \{(i,\eta_i) : \eta_i(r,t) > \delta\} \tag{7}$$

where δ is chosen to be a small positive threshold value, wherein only order parameters bigger than that are stored.

The following relations were derived for relating the simulation coefficients to the grain boundary energy, γ_{gb}, and grain boundary mobility, M_{gb}, as follows [54]:

$$\kappa = \frac{3}{4}\gamma_{gb}l_{gb} \tag{8}$$

$$\mathrm{L} = \frac{4M_{gb}}{3l_{gb}} \tag{9}$$

$$m_0 = \frac{6\gamma_{gb}}{l_{gb}} \tag{10}$$

where l_{gb} is the grain boundary width, which is a model parameter.

The boundary mobility for high angle grain boundaries (HAGB), M_{gb} $\left(\mathrm{m^4J^{-1}s^{-1}}\right)$, is defined as follows [62]:

$$M_{gb} = M_0 \exp\left(\frac{-Q_b}{RT}\right) \tag{11}$$

where Q_b is the activation energy for the migration of a HAGB, R is the universal gas constant, and M_0 is the pre-exponential factor. In view of the solute drag effect, the strain rate also has an effect on grain boundary mobility. Therefore, M can be improved as follows [63].

$$M_{gb} = \dot{\varepsilon} M_0 \exp\left(\frac{-Q_b}{RT}\right) \tag{12}$$

The parameters used for the simulation are listed in Table 2.

Table 2. Material properties of the AZ31 magnesium alloy employed in the phase-field model.

Parameter	Value	Parameter	Value
Q_{act} $\left[\mathrm{kJ\ mol^{-1}}\right]$	134 [51]	ρ_0 $\left[\mathrm{m^{-2}}\right]$	10^{10} [51]
Q_b $\left[\mathrm{kJ\ mol^{-1}}\right]$	121.791 [51]	ρ_c $\left[\mathrm{m^{-2}}\right]$	2.14×10^{14}
R $\left[\mathrm{J\ mol^{-1}K^{-1}}\right]$	8.314	k_1 $\left[\mathrm{m^{-1}}\right]$	3.88×10^{9} [51]
M_{gb} $\left(\mathrm{m^4J^{-1}s^{-1}}\right)$	1.7×10^{-13} [17]	k_2	153.37 [51]
γ_{gb} $\left[\mathrm{J\ m^{-2}}\right]$	0.332 [64]	$\Delta x = \Delta y$ [µm]	0.26
G [GPa]	14.7 [41]	Δt [s]	5×10^{-2}
b $\left[\mathrm{\AA}\right]$	3.21 [65]	l_{gb} [µm]	$4\Delta x$
l [µm]	0.363 [64]	δ	10^{-6}
τ [N]	6.82×10^{-10} [64]	r_{seed}	$14.5\Delta x$
C	8.5×10^{18} [51]		

The phase-field method's inherent diffuse interface necessitates the creation of a finite width at grain boundaries for initial microstructural representation in discontinuous dynamic recrystallization simulations. To prevent artificial changes in grain area during this process, which is especially critical for small grains, a fine grid resolution was implemented. This ensured that the diffuse interface's characteristic length scale remained substantially smaller than the minimum grain size, thus avoiding numerical dissolution of small grains, which results from the interface width becoming comparable to or larger than grain dimensions. Consequently, to achieve this resolution, the grid size was set to 940×940, and the grid spacing, Δx, considering the scale of the original microstructure and the phase-field grid, was set to 0.266 µm. To ensure sufficient numerical resolution across the diffuse interface, the grain boundary width, l_{gb}, was set to $4\Delta x$. The simulation time step, Δt, was set to 5×10^{-2} (s) to maintain numerical stability during simulation. The 2D microstructure evolution was computed at each grid point using finite difference, with an eighth-order scheme for spatial derivatives and the Euler forward method for time integration.

A unique order parameter field was generated for each grain, wherein regions occupied by grains were assigned a value of 1, and the remaining regions were assigned a value of 0. This binary field represented the initial sharp interface condition. To initiate diffuse interface formation, a brief temporal evolution of the order parameter field was performed according to Equation (6). This evolution was terminated upon the attainment of

a symmetric diffuse interface profile, ensuring a consistent representation of grain boundaries throughout the microstructure. Figure 4 illustrates the processed microstructure, visualized using order parameters and Equation (13) [66]. As shown, the diffuse interfaces are accurately formed throughout the simulation domain.

$$\varphi(r,t) = \sum_{i=1}^{g} \eta_i^2(r,t) \tag{13}$$

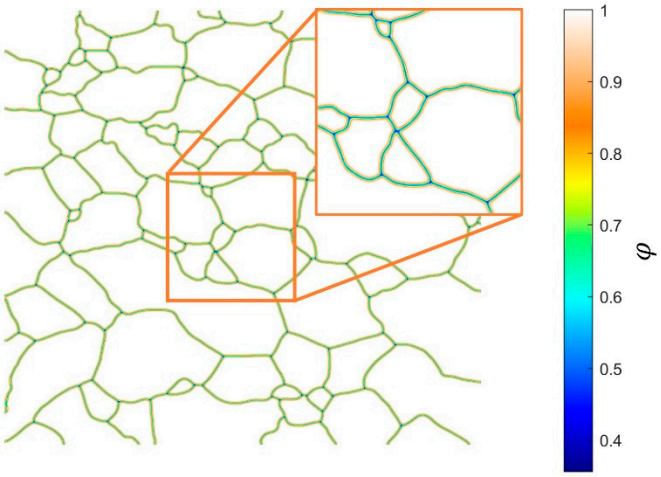

Figure 4. Grain topology of the microstructure showing diffuse interface development after holding time in phase-field model.

3.1. Dislocation Density Evolution

During thermomechanical processing, the dislocation density evolves as a result of the dynamic interaction between work hardening (WH), dynamic recovery (DRV), and dynamic recrystallization (DRX) [67,68]. Initially, work hardening, driven by dislocation generation and entanglement, causes an increase in flow stress with strain. Subsequently, dynamic recovery, involving dislocation slip and climb [69], counteracts the stress increase from work hardening. Finally, dynamic recrystallization commences when the dislocation density (ρ) reaches a critical value (ρ_c), determined by the following [70]:

$$\rho_c = \left(\frac{20\gamma_{gb}\dot{\varepsilon}}{3blM_{gb}\tau^2} \right)^{1/3} \tag{14}$$

where $\dot{\varepsilon}$ is the strain rate, l is the mean free path of the dislocation, and τ is the linear energy of the dislocation. Dynamic recrystallization induces a substantial decrease in dislocation density within newly formed grains through dislocation annihilation, leading to flow stress softening [71,72]. Therefore, the observed flow stress behavior during hot deformation is a result of the competing mechanisms of work hardening (WH), DRV, and DRX. The Kocks–Mecking (KM) model provides a framework for describing the relationship between true strain (ε) and local dislocation density (ρ_g) within a grain, incorporating dislocation accumulation from plastic deformation and dynamic recovery, as expressed by the following:

$$\frac{d\rho_g}{d\varepsilon} = k_1\sqrt{\rho_g} - k_2\rho_g \tag{15}$$

where k_1 is the WH coefficient related to the accumulation of statistically stored dislocations (SSDs) [73], and k_2 is the dynamic recovery coefficient dependent on temperature (T) and strain rate [16]. Within the framework of the proposed phase-field model, the local dislocation density (ρ_g) is treated as a spatially homogeneous variable within the confines

of each individual grain constituting the microstructure. Consequently, the model does not incorporate any spatial heterogeneity or distribution of dislocation density within a single grain.

Due to the similarities in composition and processing conditions between the AZ31 Mg alloy used in this study and that investigated by Liu et al. [51], all relevant material parameters, including the Kocks–Mecking coefficients, were adopted from their work. By utilizing the well-established parameters from Liu et al., the model benefits from validated data, thereby reducing uncertainties associated with material property estimation. This approach ensures that the mechanical responses of the AZ31 Mg alloy in the simulations align closely with experimentally observed behavior, enhancing the predictive accuracy of the study.

3.2. Nucleation Process

Experimental observations have shown that during uniform deformation, nucleation events preferentially initiate at triple junctions and grain boundaries, rather than within grain interiors [56]. This preference is attributed to the energetically favorable nucleation sites provided by triple junctions, which possess a higher grain boundary area-to-volume ratio [74,75]. Therefore, these established assumptions are incorporated into the present investigation. Specifically, in this study, nuclei are placed exclusively at triple junctions and grain boundaries, with their spatial distribution randomized.

A circular nucleus, centered at the selected position, is introduced into the simulation domain. The initial order parameter within this nucleus is governed by the following function [22]:

$$\eta_i = \frac{1}{2}\left(1 - \tanh\left(\frac{d - r_{seed}}{2\Delta x}\right)\right) \tag{16}$$

where d represents the radial distance from the center of the nucleus, r_{seed} denotes the radius of the nucleus, and Δx is the grid spacing. Following the introduction of nuclei into the phase-field domain, an initial relaxation period is necessary to allow the microstructure to adjust to the newly formed recrystallized grains [76,77]. This requirement addresses the potential for non-physical artifacts due to overlapping order parameters. It is noteworthy that this methodology is applicable to static recrystallization (SRX) simulations. In such simulations, the holding process, which precedes SRX, can be excluded from the computational domain, thereby not affecting the main microstructure evolution. However, in discontinuous dynamic recrystallization modeling, the coupled processes of deformation and nucleation necessitate a different approach. Incorporating a holding time for nuclei stabilization at each nucleation step is not only computationally inefficient but may also induce microstructural artifacts, such as anomalous grain growth. To circumvent this issue, a two-grain simulation was conducted utilizing identical material and model parameters as the primary simulation. The diffuse interface profile of the order parameters at the grain boundary was then extracted. Subsequently, a fitting procedure was performed on the r_{seed} parameter to ensure the seed order parameter accurately replicated the simulated diffuse interface profile, as depicted in Figure 5. Finally, during the primary simulation, upon insertion of each nucleus into the microstructure, the existing order parameters within the nucleus's spatial domain were replaced with an exact copy (a replica, Grain B in Figure 5) of the nucleus's order parameter profile. This procedure effectively eliminated the requirement for a holding time to establish a symmetrical diffuse interface at grain boundaries.

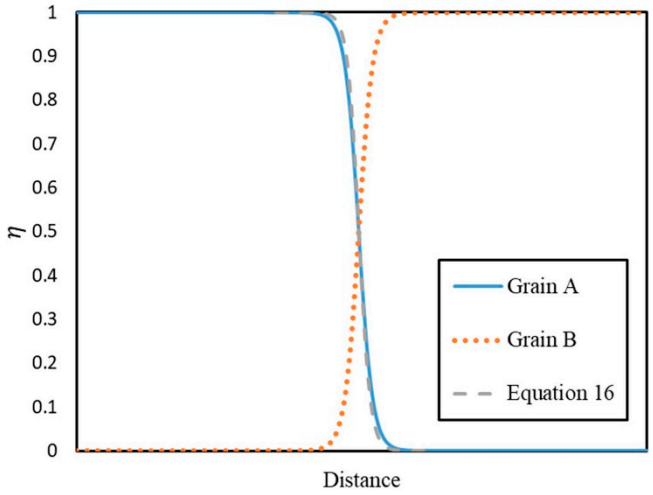

Figure 5. Diffuse interface development in the simulation of two-grain model with fitted r_{seed} in the Equation (16).

Given the determination of nuclei position, size, and order parameter, the quantity of nuclei introduced per time increment into the dynamically evolving microstructure is directly proportional to the nucleation rate. Ding and Guo [16] used the following equation for the nucleation rate:

$$\dot{n} = C\dot{\varepsilon}\exp\left(\frac{-Q_{act}}{RT}\right) \tag{17}$$

where C is a material fitting coefficient. Nucleation is initiated at a discrete grid node when the local dislocation density (ρ) attains the critical value (ρ_c). Upon reaching this threshold, a stochastic nucleation event occurs, introducing a quantity of nuclei (dn), as defined by Equation (18) [78], into the microstructure at each discrete time step. The placement of these nuclei within the microstructure is randomized, simulating the inherent randomness of nucleation phenomena.

$$dn = \frac{\dot{n}\Delta t n_{gb}\Delta x\Delta y}{l_{gb}} \tag{18}$$

where dn represents the nucleation number, and n_{gb} representing the count of discrete grid points defining grain boundaries.

3.3. Grid Deformation Model

The deformation occurring during discontinuous dynamic recrystallization is approximated by altering the simulation grid dimensions. Takaki et al. [27] employed the relationship between nominal strain and true strain to calculate the grid dimension in the y-direction and subsequently determined the grid dimension in the x-direction by maintaining a constant simulation area. While this method is suitable for simulating uniaxial compression straining, it is not directly applicable to modeling the impression creep process. To address this limitation, the results from an upper-bound analysis of the impression creep test [44] are utilized. Specifically, the relationship between strain rate ($\dot{\varepsilon}$) and impression rate ($\dot{U}$), derived assuming a constant friction factor of 0.35, is employed. Based on the value of this constant friction factor, the ratio of impression rate to strain rate ($\dot{U}/\dot{\varepsilon}$) can be calculated and used to determine the impression depth, U, as follows.

$$U = \left(\frac{\dot{U}}{\dot{\varepsilon}}\right) \times \varepsilon \tag{19}$$

The indenter displacement, representing the impression depth, is imposed on the simulation grid along the y-axis. To enforce volume conservation within the two-dimensional simulation domain during plastic deformation, the spatial discretization along the x-axis is dynamically scaled. This scaling factor is determined by the inverse ratio of the current y-dimension to the initial y-dimension, thereby ensuring that the total area of the computational domain remains invariant throughout the deformation process.

4. Dynamic Recrystallization During the Impression Creep Testing

Dynamic recrystallization is a critical phenomenon during high-temperature creep deformation, especially in materials with low stacking fault energy where recovery rates are slow, allowing sufficient stored energy to accumulate for new grain nucleation and growth. As evidenced in pure Pb, Ni, austenite [79], and complex alloys like Nimonic 108 [80,81], DRX induces significant softening through dislocation annihilation within newly formed grains, leading to a rapid increase in creep rate [82], often punctuated by oscillations [34,83]. This softening is manifested as a pronounced stress drop in stress–strain curves, reflecting the influence of DRX kinetics and the resulting microstructure on the rate at which recrystallization occurs. The process commences only when a critical strain, dependent on stress and temperature, is exceeded, with the critical strain generally decreasing with increasing stress and temperature. Impurities can also elevate the strain required for recrystallization [82]. The interplay between the initial microstructure and the evolution of recrystallized grains, coupled with the formation and growth rate of strain-free grains under applied stress, dictates the creep behavior, highlighting the fundamental link between DRX dynamics and the macroscopic mechanical response of materials during high-temperature deformation.

Figure 6a illustrates schematic creep curves depicting the influence of dynamic recrystallization during conventional tensile creep testing. In the absence of DRX, the expected stages of primary, secondary (steady-state), and tertiary creep are clearly observable. Conversely, the occurrence of DRX manifests as a discernible increase in creep rate immediately following the establishment of steady-state conditions [82]. This behavior underscores the softening effect of DRX on the material's creep resistance. Consistent with the observations in tensile creep, dynamic recrystallization is also seen in impression creep tests [47,84]. Analogously, Figure 6b demonstrates a similar phenomenon in impression creep curves, where an elevated impression rate is observed post-DRX initiation. This increase in impression rate reflects the localized softening induced by DRX within the impression zone, mirroring the macroscopic creep rate enhancement observed in conventional creep testing.

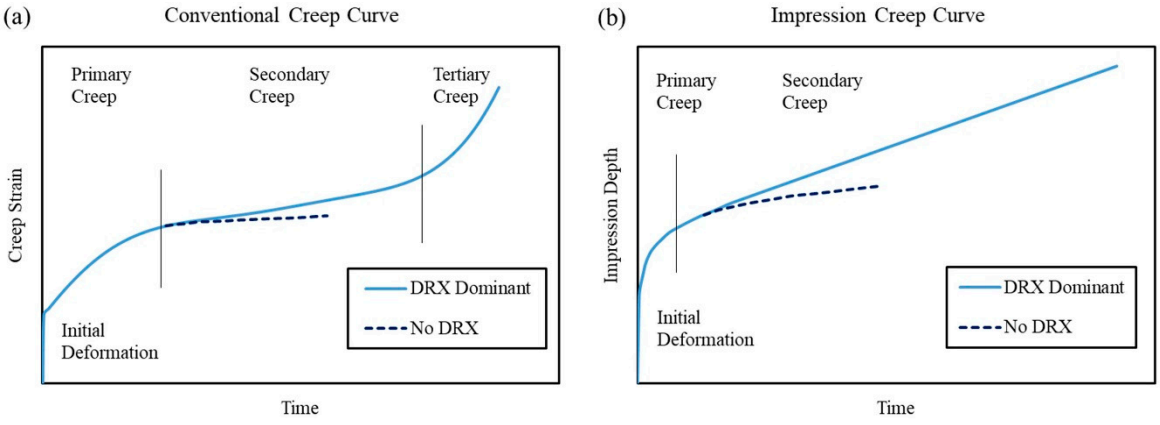

Figure 6. Schematic representation of creep curves illustrating the influence of dynamic recrystallization (DRX): (**a**) conventional tensile creep curve demonstrating the DRX-induced accelerated creep; (**b**) impression creep curve showing the increase in impression rate following the initiation of DRX.

Creep and hot deformation are distinct high-temperature deformation processes, primarily differentiated by their loading conditions and experimental methodologies. In creep, a constant external stress is applied, and the resulting strain is monitored as a function of time, characterizing the material's time-dependent deformation behavior. Conversely, hot deformation involves imposing a constant strain rate, with the corresponding stress response being measured. This fundamental difference in loading protocols—constant stress in creep versus constant strain rate in hot deformation—manifests as divergent macroscopic mechanical responses and testing procedures. However, at the microscopic level, both processes exhibit fundamental similarities in dislocation activity and plastic deformation mechanisms. Thus, despite the macroscopic variations in loading, the underlying microscopic mechanisms of plastic deformation remain essentially consistent [35]. Consequently, due to this shared microscopic basis, the Kocks–Mecking model, which effectively describes dislocation-mediated plastic deformation, can be applied to model both creep and hot deformation processes.

In conventional dynamic recrystallization modeling, such as for hot compression processes [27], a constant strain rate is typically imposed. With a fixed time increment (Δt), the incremental strain ($d\varepsilon$) is calculated. Consequently, given the constancy of both strain rate and Δt, $d\varepsilon$ remains constant throughout the simulation. Utilizing the Kocks–Mecking relationship (Equation (15)), the incremental dislocation density ($d\rho$) is computed within the deformed grains at each time step. This iterative process continues until the dislocation density reaches the critical value (ρ_c), triggering the initiation of nucleation. The stress at each time step can then be determined using the following [27]:

$$\sigma = \alpha G b \sqrt{\rho_{mean}} \tag{20}$$

where α is a dislocation interaction coefficient of approximately 0.5. During nucleation, the dislocation density within the newly formed nuclei is substantially lower than that of the surrounding deformed grains, leading to a reduction in the average dislocation density (ρ_{mean}) and consequently, a decrease in stress. However, in creep processes, stress is maintained constant, and the strain rate is an unknown variable, rendering the incremental strain ($d\varepsilon$) indeterminate. Nevertheless, during nucleation, the incremental dislocation density is determined by the difference between the average dislocation density of the microstructure prior to and following the nucleation event, $d\rho_{mean}$. By rearranging the Kocks–Mecking relationship, the incremental strain can be calculated as follows.

$$d\varepsilon = \frac{d\rho_{mean}}{k_1 \sqrt{\rho_{mean}} - k_2 \rho_{mean}} \tag{21}$$

From the incremental strain data, the strain rate is calculated using the Δt and $d\varepsilon$. Subsequently, these derived parameters are transformed into impression depth and impression velocity via Equation (19), enabling the construction of the impression depth versus time curve. Nevertheless, the initial instantaneous deformation and strain rate prior to discontinuous dynamic recrystallization remain unknown.

The instantaneous deformation can be estimated using finite element analysis. In this study, the primary creep rate is neglected due to the limited extent of the primary creep region in impression creep processes [39]. The initial steady-state creep rate (before DDRX) can be estimated based on existing literature, and the critical dislocation density for discontinuous dynamic recrystallization is assumed to be consistent with that used in hot compression simulations (Equation (14)). Utilizing this configuration, the dislocation density evolution can be predicted under a constant strain rate, employing a methodology analogous to compression deformation modeling, until the critical dislocation density

is attained. Following the onset of nucleation, Equation (21) is used to calculate $d\varepsilon$ and the strain rate. This process continues until complete microstructural recrystallization is achieved. Consequently, the steady-state creep rate in the impression creep process can be predicted.

5. Simulation Stages

The numerical procedure for the developed phase-field discontinuous dynamic recrystallization (PF-DDRX) model is illustrated in the flow chart presented in Figure 7. Dislocation activity is modeled through the dynamic competition between work hardening, dynamic recovery, and DDRX, as described in Section 3.1. Recrystallization grains nucleate according to the mechanisms outlined in Section 3.2. The deformation stored energy, acting as an additional driving force in the PF-DDRX model, interacts with grain boundary energy to govern the evolution of deformed (DEF) and recrystallized (DRX) grains, as detailed in Section 3. These simulations provide insights into microstructural evolution and its influence on macroscopic mechanical responses during impression creep, as well as DRX kinetics.

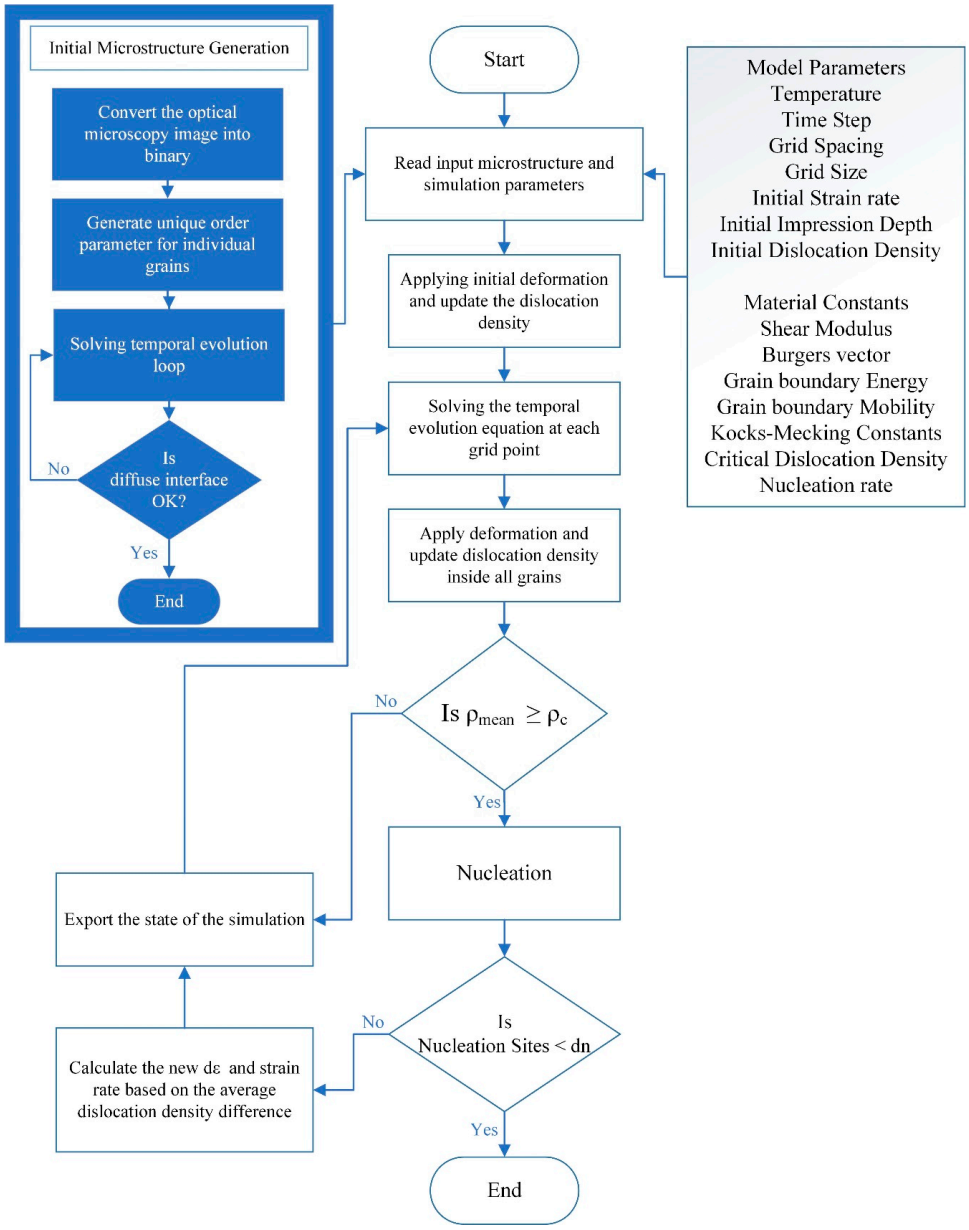

Figure 7. Flow chart of the simulation scheme.

The simulation process comprises the following sequential steps:

1. **Initial Microstructure Generation:** An initial order parameter field is generated from an optical microscopy microstructure image.
2. **Parameter Initialization:** All model and material parameters are input into the simulation.
3. **Initial Deformation and Dislocation Density Calculation:** The initial deformation, obtained from finite element analysis (FEA), is applied to the simulation grid, and the corresponding dislocation density inside each grain in the microstructure is calculated.
4. **Microstructure and Dislocation Evolution Loop:** A loop iterates through the grain dislocation evolution, simulating the interplay of WH, DRV, and DRX.
5. **Stochastic Nucleation:** Nucleation occurs stochastically at eligible grain boundaries.
6. **Incremental Strain and Strain Rate Calculation:** After each nucleation event, the incremental strain and strain rate are calculated, and the values are updated for the next iterative step.
7. **Iteration Continuation:** The simulation monitors the fraction of recrystallized volume at each evolution loop and terminates when complete recrystallization is attained.

6. Results and Discussion

Figure 8 presents the experimental impression creep curve for the AZ31 magnesium alloy, revealing an instantaneous deformation depth of approximately 63 μm at the test's onset. Finite element analysis (FEA), employing material properties and boundary conditions consistent with the experimental setup (250 °C and a constant impression pressure of 200 MPa), yielded an instantaneous impression depth of approximately 70 μm, as illustrated in Figure 9. While precise measurement of the instantaneous deformation depth is challenging in experimental investigations due to factors such as thermal expansion and the micrometer-scale nature of the deformation, the FEA result demonstrates reasonable agreement with the experimental data. In accordance with Section 3.3, the FEA-derived impression depth was first transformed into strain via Equation (19). Subsequently, this calculated strain, together with ρ_0, was applied to Equation (15) to compute the initial average dislocation density, ρ_{ini}, within the grains. The instantaneous impression depth and the calculated average dislocation density were then applied as the initial conditions for the microstructure in the main temporal evolution loop of the phase-field simulation.

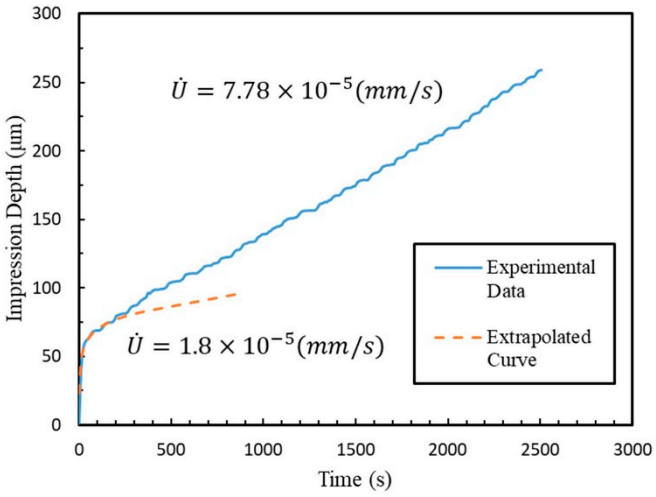

Figure 8. Experimental impression creep data for AZ31 alloy at 250 °C and a constant stress of 200 MPa.

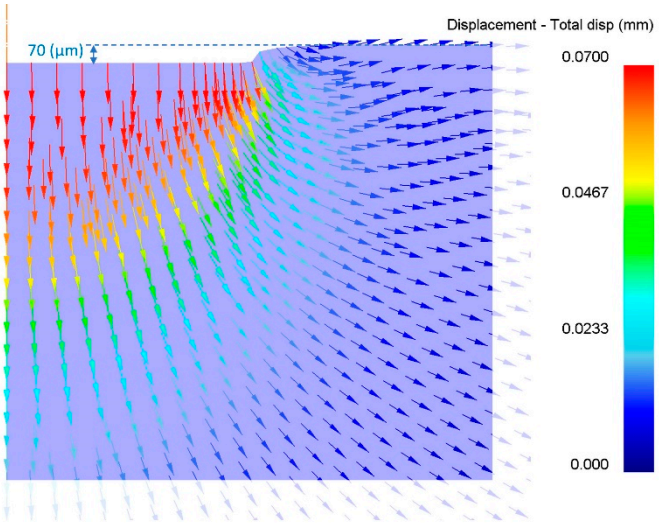

Figure 9. Finite element analysis (FEA) results illustrating the predicted instantaneous indentation depth and total displacement contours (shown as vector plot), with boundary conditions matching the experimental temperature and applied stress.

Figure 8 illustrates that extrapolating a fitted curve from the initial stage of the experimental data, where recrystallization is absent, to later times yields a slope (impression rate) lower than that observed in the steady-state region. This discrepancy in slope is attributed to softening induced by discontinuous dynamic recrystallization (DDRX). The fitted and experimental curves exhibit perfect overlap until approximately 190 s, marking the onset of DDRX.

Using the conversion factors from the upper-bound analysis of the deformation zone in the impression creep test [44], the impression pressure and the impression rate can be converted to the equivalent tensile creep stress and strain rate, respectively, according to

$$\sigma = \eta P \tag{22}$$

$$\dot{\varepsilon} = \beta \dot{U} \tag{23}$$

where η and β are the correlation factors for the stress and strain rate, respectively. The stress conversion factor for the AZ31 alloy was calculated to be 0.26, and the strain rate conversion factor was calculated using a suitable velocity field to be 2.22 according to the instructions detailed in [44]. The impression pressure was converted to stress using Equation (22). Subsequently, the steady-state creep strain rate was determined via the Friedel model [41,85], yielding a value of 3.84×10^{-5} $(1/\mathrm{s})$. This strain rate was then converted to a value of 1.73×10^{-5} $(\mathrm{mm/s})$ using Equation (23) and the declared correlation factor. This calculated strain rate is in close agreement with the fitted impression rate observed in Figure 8. To better optimize the computation of grid size variations during creep deformation, the calculated strain rate value was rounded to 4×10^{-5} $(1/\mathrm{s})$ and adopted as the initial strain rate for the simulation.

Utilizing the established initial simulation configuration, the temporal evolution of deformation in the AZ31 magnesium alloy during impression creep was simulated. Figure 10 presents a comparison between the impression depth versus time curves predicted by the PF-DDRX model and those obtained experimentally. The results indicate that the steady-state impression rate is accurately predicted by the phase-field model. Specifically, the predicted value (8.19×10^{-5} mm/s) demonstrates close agreement (about 5% error) with the experimental steady-state impression rate (7.78×10^{-5} mm/s). Furthermore, the predicted onset of DDRX at 223 s aligns reasonably with the experimental observation

of 190 s. These findings confirm a strong correlation between the predicted initial impression depth derived from finite element modeling, the calculated initial impression rate, and empirical observations. Distinctly, the critical indentation depth for the initiation of discontinuous dynamic recrystallization can be identified as the point at which the average dislocation density within the microstructure attains the critical dislocation density, as determined by Equation (14), exhibiting good agreement with experimental observations (73 μm predicted vs. 75 μm measured). The observed deviation between the simulated and experimental creep curves during the initial transient period (t < 100 s) is attributed to the model's inherent assumption of negligible primary creep, which is typically not critical in creep design. The simulation initiates with an idealized, pre-established deformation volume and an instantaneous attainment of a constant creep strain rate, contrasting with the gradual microstructural development characteristic of experimental primary creep. This simplification was implemented to specifically investigate the steady-state creep regime, which constitutes the primary objective of this study. Consequently, while the initial kinetics are not fully captured, this assumption is not anticipated to significantly compromise the accuracy of the predicted steady-state creep rate and the underlying microstructural evolution mechanisms.

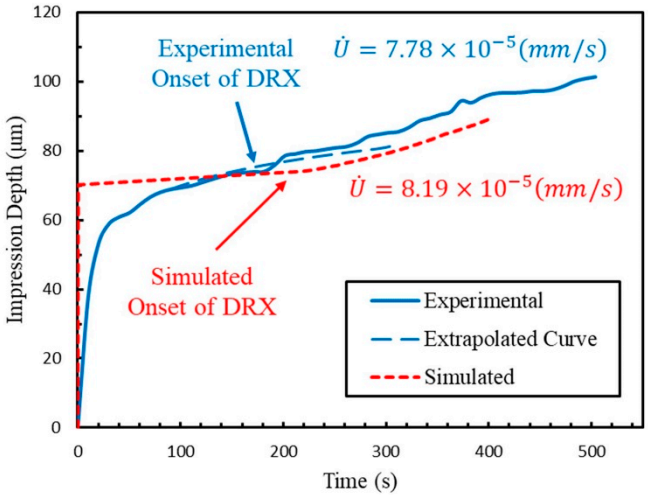

Figure 10. Simulated impression creep curve for the AZ31 alloy at 250 °C and a constant stress of 200 MPa.

Figure 11 illustrates the microstructural evolution during impression creep at 250 °C and 200 MPa, demonstrating the progression of discontinuous dynamic recrystallization with increasing indentation depth. In this figure, white regions represent initial grains, colored regions represent recrystallized grains, and lines delineate grain boundaries. Figure 11a depicts the initial microstructure prior to the onset of nucleation, where the dislocation density within the grains reaches the critical value. Figure 11b–e present the simulated microstructural evolution of discontinuous dynamic recrystallization as it occurs within the impression creep process.

The left column of Figure 11 showcases the evolution of the microstructure, while the right column presents the corresponding grain size distribution histograms. Initially, nuclei formation commences at the original grain boundaries (Figure 11b). Subsequently, new grains nucleate at the boundaries of previously recrystallized grains, leading to the formation of necklace-like structures characteristic of DRX-induced grain refinement (Figure 11c–e).

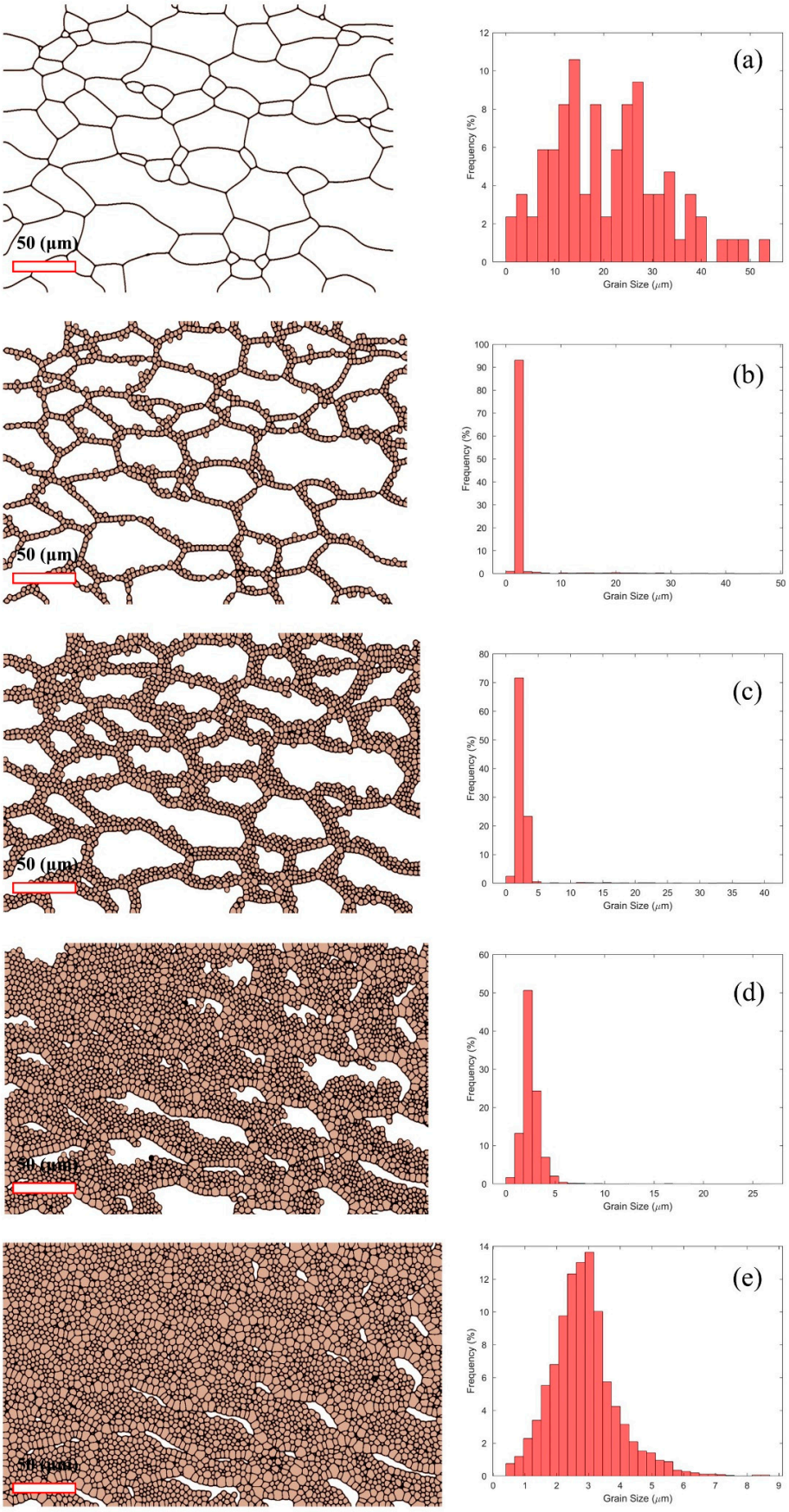

Figure 11. Simulated microstructural and grain size evolution with increasing depth and time during impression creep (250 °C, 200 MPa): (**a**) 73 μm (200 s), (**b**) 76 μm (260 s), (**c**) 79 μm (300 s), (**d**) 85 μm (360 s), and (**e**) 89 μm (400 s).

Analysis of the corresponding grain size distribution histograms (right column of Figure 11) reveals a progressive shift towards smaller grain sizes as DRX progresses. Initially, the grain size distribution exhibits a relatively broad range with a peak in the larger grain size region (Figure 11a). As DRX initiates and new grains form at the original grain boundaries (Figure 11b), a slight shift towards smaller grain sizes is observed. With further strain accumulation and the nucleation of new grains at the boundaries of previously recrystallized grains (Figure 11c–e), the grain size distribution becomes increasingly skewed towards smaller grain sizes, indicating significant grain refinement. This refinement is consistent with the observed necklace-like structures and the gradual expansion of DRX grains into the original grains, as depicted in the left column of Figure 11. The observed refinement of the average grain size during impression creep is a direct consequence of the discontinuous dynamic recrystallization (DDRX) mechanism, wherein the continuous nucleation of fine, strain-free grains leads to a progressive decrease in the overall grain size of the microstructure. The microstructural evolution observed in the left column of Figure 11, which illustrates the formation of the necklace-like structures of recrystallized grains and their subsequent encroachment upon the original, deformed grains, supports this as well.

Figure 12 illustrates the predicted temporal evolution of the DDRX fraction and average grain size. Initially, the DDRX fraction remains at zero until 223 s, corresponding to the point at which the dislocation density inside grains attains the critical value and DDRX commences. Subsequently, the microstructure undergoes complete recrystallization by 400 s. Concurrently, the average grain size exhibits a reciprocal trend, demonstrating a rapid decrease from approximately 32.5 μm to 5.5 μm within the first 130 s following DDRX initiation, before stabilizing at 3.7 μm. This inverse correlation between DDRX fraction and grain size, consistent with observations in other studies [17,20], underscores the microstructural refinement resulting from the formation of new, smaller grains during discontinuous dynamic recrystallization.

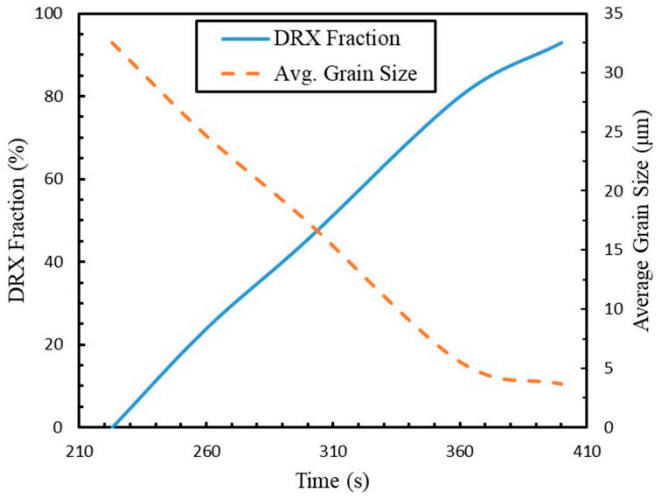

Figure 12. Discontinuous dynamic recrystallization fraction and average grain size evolution during impression creep simulation.

For the purpose of validating the simulated microstructural evolution, experimental analysis of the AZ31 magnesium alloy during impression creep testing was conducted using optical microscopy. The resulting experimental microstructures, illustrated in Figure 13, exhibit a comparable trend to those predicted by the simulation, as presented in Figure 11.

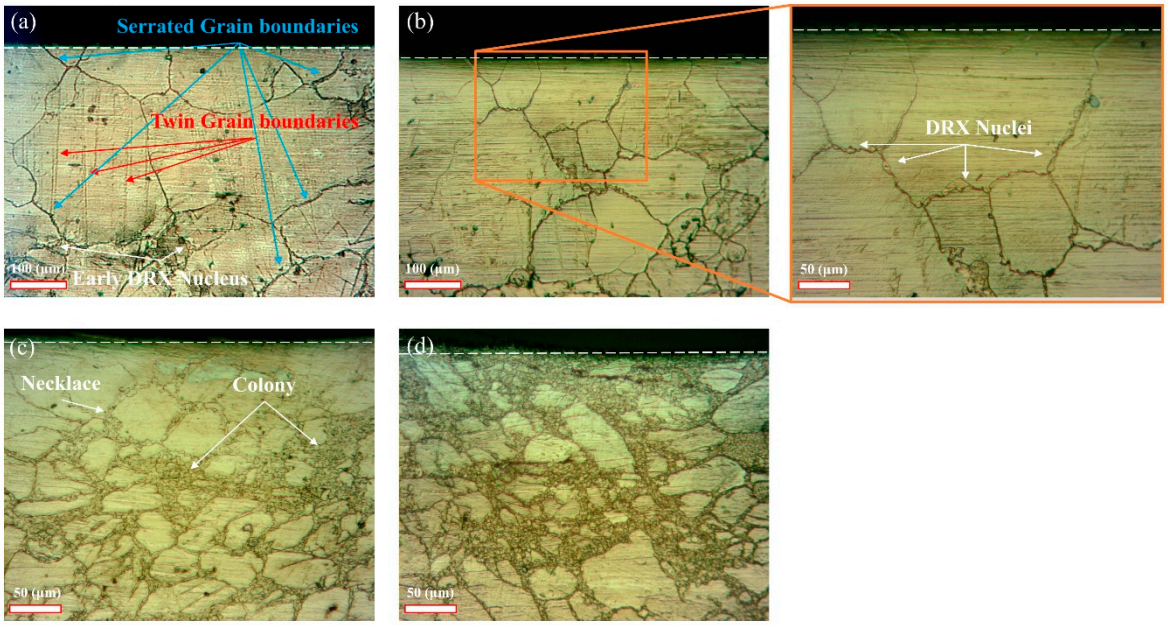

Figure 13. Experimental microstructural evolution with increasing indenter depth during impression creep (250 °C, 200 MPa) at impression depths of (**a**) 70 μm (90 s), (**b**) 75 μm (180 s), (**c**) 80 μm (270 s), and (**d**) 90 μm (380 s). The dashed white line indicates the specimen's surface.

The acquisition of the metallographic images presented herein posed significant experimental challenges. Precise measurement of impression depth was difficult, and sample preparation was a protracted process necessitating the utilization of multiple specimens. As depicted in Figure 13a, the serrated grain boundaries, which are known to be susceptible to dynamic recrystallization (DRX) [86,87], exhibit no discernible evidence of DRX at an impression depth of 80 μm. However, a limited number of DRX nuclei are observed at triple junctions, where the elevated grain boundary area-to-volume ratio appears to promote recrystallization at dislocation densities below the critical threshold [74,75]. Subsequently, the DRX process is initiated, with nuclei formation occurring along grain boundaries, resulting in the characteristic necklace structure observed in Figure 13b. Further progression of the DRX process, as illustrated in Figure 13c,d, is characterized by the gradual development of nucleation into the grain interiors, culminating in the formation of DRX grain colonies [88]. Figure 14a,b present the fully recrystallized microstructure of the AZ31 magnesium alloy, along with an enlarged selected area for detailed microstructural analysis, respectively. The grain size distribution presented in Figure 14c exhibits a close correlation between experimental and simulated data. Furthermore, the measured average grain size of 3.16 μm demonstrates good agreement with a predicted value of 3.7 μm. This concordance validates the selected material parameters and model parameters, including the seed radius (r_{seed}) and grid spacing and size, confirming their consistency with experimental observations.

Figure 16 presents a series of assembled microstructure images, obtained from a specimen subjected to an impression depth of approximately 450 μm, to investigate a larger area in the vicinity of the indenter.

The region immediately adjacent to the indenter exhibits the earliest complete recrystallization during discontinuous dynamic recrystallization, a consequence of the elevated strain and stress concentrations prevalent in this area. With increasing impression depth, the strain field expands, and the DRX zone propagates to encompass the larger surrounding regions of the initially recrystallized microstructure.

Areas characterized by smaller grain sizes demonstrate accelerated recrystallization kinetics compared to larger grains. This phenomenon is attributed to the higher dislocation

density within smaller grains at a given strain, coupled with their increased grain boundary-to-volume ratio, which promotes rapid nucleation and growth.

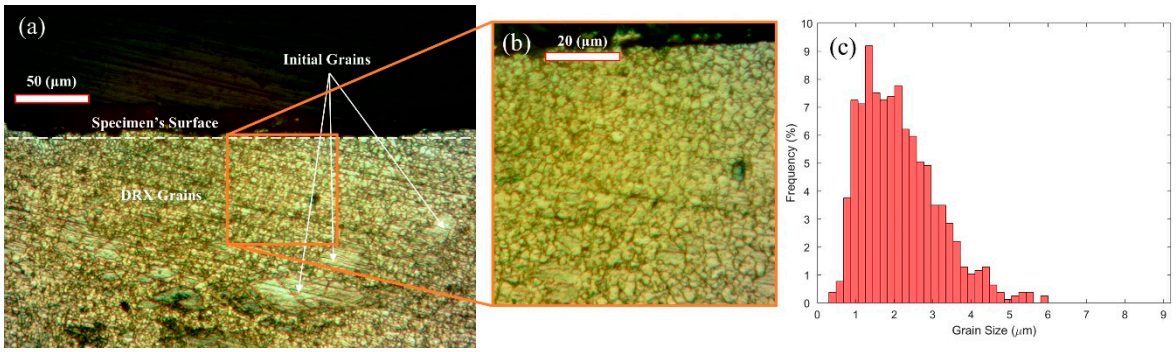

Figure 14. Microstructure of AZ31 showing complete recrystallization at 100 μm impression depth: (**a**) microstructure image, (**b**) magnified view of the selected region in (**a**), and (**c**) grain size distribution histogram.This study has demonstrated that the developed phase-field model accurately predicts both the steady-state impression rate and the discontinuous dynamic recrystallization microstructural evolution during impression creep testing of the AZ31 magnesium alloy. To further elucidate the DRX phenomenon within this context, microstructural analysis was conducted at progressively increasing impression depths. As the indenter penetrates deeper into the specimen during the impression creep process, the DRX regime extends to greater depths and encompasses wider spatial areas, as illustrated in Figures 15 and 16. The microstructure beneath the DRX colony, indicative of the incipient stage of discontinuous dynamic recrystallization, exhibits a necklace-like structure.

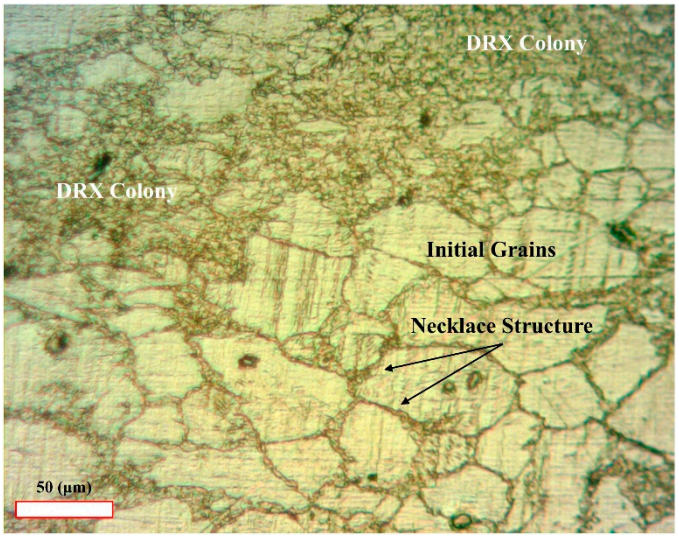

Figure 15. Experimental microstructural evolution of AZ31 after impression creep testing, focusing on lower observation depths.

Conversely, larger grains exhibit elevated dislocation densities near their grain boundaries due to the accumulation of geometrically necessary dislocations (GNDs), facilitating the rapid formation of necklace structures. However, their lower intragranular dislocation density and larger grain volume result in delayed recrystallization, necessitating higher strains for completion. The increased grain volume and lower average dislocation density in larger grains contribute to this delayed recrystallization. As observed in the enlarged region depicted in Figure 16, the DRX colony forms beneath larger grains, despite the average strain in the upper zone exceeding that of the colony zone.

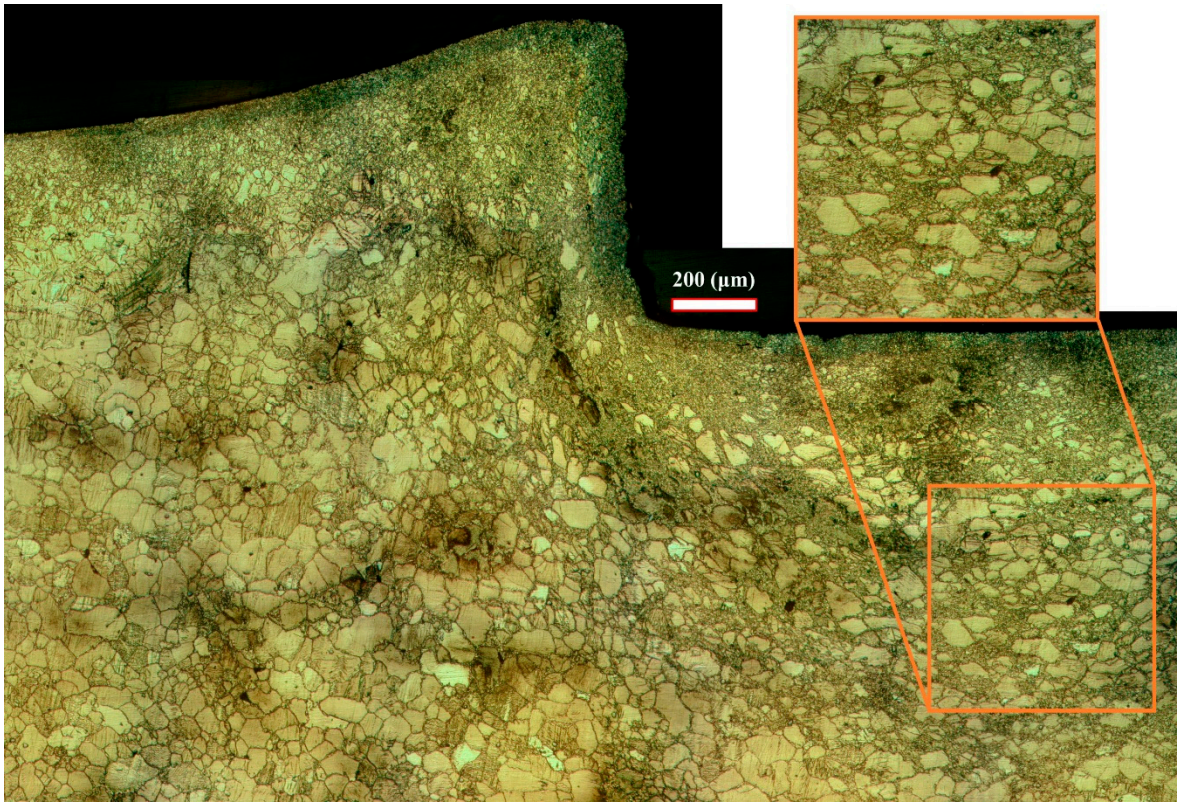

Figure 16. Assembled microstructure images of AZ31 after impression creep at an impression depth of 450 μm.

7. Conclusions

This study developed and validated a phase-field model, coupled with the Kocks–Mecking (KM) dislocation density evolution theory, to predict the steady-state creep rate and microstructural evolution of the AZ31 magnesium alloy during discontinuous dynamic recrystallization (DDRX) in impression creep testing. Key findings and contributions are summarized below:

1. An algorithm was implemented to extract the initial grain structure directly from optical microscopy images of the homogenized microstructure. Finite element analysis (FEA) was then employed to determine the instantaneous deformation, and the resulting impression depth was applied as the initial condition for the phase-field model.
2. Model parameters, including hardening and softening coefficients related to dislocation activity, grain boundary energy, and mobility, were obtained from existing literature.
3. The predicted impression creep rate of 8.19×10^{-5} mm/s demonstrated good agreement with the experimentally measured rate of 7.78×10^{-5} mm/s.
4. The predicted average grain size of the fully recrystallized microstructure was 3.7 μm, which also showed good agreement with the experimental observation of 3.16 μm.
5. The predicted recrystallization kinetics and grain topology evolution demonstrated excellent agreement with experimental observations, validating the model's predictive capability for microstructure evolution.

The proposed phase-field model offers a reliable and accurate approach for predicting the steady-state creep rate, grain size distribution, and microstructural evolution during DDRX in the AZ31 magnesium alloy. This methodology provides valuable insights for

lifetime prediction and microstructure development in this material under impression creep conditions.

Building upon the insights gained from this two-dimensional phase-field model, future research endeavors could significantly benefit from extending the current framework to three-dimensional simulations. Such an expansion would enable a more comprehensive and spatially resolved understanding of the complex microstructural evolution during discontinuous dynamic recrystallization.

Author Contributions: Conceptualization, R.E.; methodology, A.R. and R.E.; software, A.R.; validation, A.R. and R.E.; formal analysis, A.R.; investigation, A.R.; resources, R.E. and E.B.; data curation, A.R.; writing—original draft preparation, A.R.; writing—review and editing, R.E. and E.B.; visualization, A.R.; supervision, R.E.; project administration, R.E.; funding acquisition, R.E. and E.B. All authors have read and agreed to the published version of the manuscript.

Funding: This research was funded by the Research Council of Shiraz University, grant number 99-GR-ENG 15. The APC was funded by Brunel University of London.

Data Availability Statement: The data presented in this study are not publicly available at this time as they form part of an ongoing research project. Data may be made available in the future upon reasonable request and after the completion of the related study.

Conflicts of Interest: The authors declare no conflicts of interest.

References

1. Fatemi-Varzaneh, S.M.; Zarei-Hanzaki, A.; Beladi, H. Dynamic recrystallization in AZ31 magnesium alloy. *Mater. Sci. Eng. A* **2007**, *456*, 52–57. [CrossRef]
2. Yang, X.-Y.; Ji, Z.-S.; Miura, H.; Sakai, T. Dynamic recrystallization and texture development during hot deformation of magnesium alloy AZ31. *Trans. Nonferrous Met. Soc. China* **2009**, *19*, 55–60. [CrossRef]
3. He, D.-G.; Lin, Y.C.; Chen, M.-S.; Li, L. Kinetics equations and microstructural evolution during metadynamic recrystallization in a nickel-based superalloy with δ phase. *J. Alloys Compd.* **2017**, *690*, 971–978. [CrossRef]
4. Maghsoudi, M.H.; Zarei-Hanzaki, A.; Changizian, P.; Marandi, A. Metadynamic recrystallization behavior of AZ61 magnesium alloy. *Mater. Des.* **2014**, *57*, 487–493. [CrossRef]
5. Ullmann, M.; Graf, M.; Schmidtchen, M.; Kawalla, R. Metadynamic Recrystallization Kinetics of Twin Roll Cast AZ31 Alloy during Hot Deformation. *Procedia Eng.* **2014**, *81*, 1559–1564. [CrossRef]
6. Chao, H.Y.; Sun, H.F.; Chen, W.Z.; Wang, E.D. Static recrystallization kinetics of a heavily cold drawn AZ31 magnesium alloy under annealing treatment. *Mater. Charact.* **2011**, *62*, 312–320. [CrossRef]
7. Seyed Salehi, M.; Serajzadeh, S. Simulation of static recrystallization in non-isothermal annealing using a coupled cellular automata and finite element model. *Comput. Mater. Sci.* **2012**, *53*, 145–152. [CrossRef]
8. Yang, X.-Y.; Zhu, Y.-K.; Miura, H.; Sakai, T. Static recrystallization behavior of hot-deformed magnesium alloy AZ31 during isothermal annealing. *Trans. Nonferrous Met. Soc. China* **2010**, *20*, 1269–1274. [CrossRef]
9. Humphreys, F.J.; Hatherly, M. Chapter 13—Hot Deformation and Dynamic Restoration. In *Recrystallization and Related Annealing Phenomena*, 2nd ed.; Humphreys, F.J., Hatherly, M., Eds.; Elsevier: Oxford, UK, 2004; pp. 415–450.
10. Mirzadeh, H. Grain refinement of magnesium alloys by dynamic recrystallization (DRX): A review. *J. Mater. Res. Technol.* **2023**, *25*, 7050–7077. [CrossRef]
11. Estrin, Y. Dislocation theory based constitutive modelling: Foundations and applications. *J. Mater. Process. Technol.* **1998**, *80–81*, 33–39. [CrossRef]
12. Roters, F.; Raabe, D.; Gottstein, G. Work hardening in heterogeneous alloys—A microstructural approach based on three internal state variables. *Acta Mater.* **2000**, *48*, 4181–4189. [CrossRef]
13. Peczak, P.; Luton, M.J. A Monte Carlo study of the influence of dynamic recovery on dynamic recrystallization. *Acta Metall. Mater.* **1993**, *41*, 59–71. [CrossRef]
14. Rollett, A.D.; Luton, M.J.; Srolovitz, D.J. Microstructural simulation of dynamic recrystallization. *Acta Metall. Mater.* **1992**, *40*, 43–55. [CrossRef]
15. Goetz, R.L.; Seetharaman, V. Modeling Dynamic Recrystallization Using Cellular Automata. *Scr. Mater.* **1998**, *38*, 405–413. [CrossRef]

16. Ding, R.; Guo, Z.X. Coupled quantitative simulation of microstructural evolution and plastic flow during dynamic recrystallization. *Acta Mater.* **2001**, *49*, 3163–3175. [CrossRef]
17. Chen, M.-S.; Yuan, W.-Q.; Li, H.-B.; Zou, Z.-H. Modeling and simulation of dynamic recrystallization behaviors of magnesium alloy AZ31B using cellular automaton method. *Comput. Mater. Sci.* **2017**, *136*, 163–172. [CrossRef]
18. Kugler, G.; Turk, R. Modeling the dynamic recrystallization under multi-stage hot deformation. *Acta Mater.* **2004**, *52*, 4659–4668. [CrossRef]
19. Wang, L.; Fang, G.; Qian, L. Modeling of dynamic recrystallization of magnesium alloy using cellular automata considering initial topology of grains. *Mater. Sci. Eng. A* **2018**, *711*, 268–283. [CrossRef]
20. Cai, Y.; Sun, C.Y.; Li, Y.L.; Hu, S.Y.; Zhu, N.Y.; Barker, E.I.; Qian, L.Y. Phase field modeling of discontinuous dynamic recrystallization in hot deformation of magnesium alloys. *Int. J. Plast.* **2020**, *133*, 102773. [CrossRef]
21. Gentry, S.P.; Thornton, K. Simulating recrystallization in titanium using the phase field method. *IOP Conf. Ser. Mater. Sci. Eng.* **2015**, *89*, 012024. [CrossRef]
22. Gentry, S.P.; Thornton, K. Sensitivity analysis of a phase field model for static recrystallization of deformed microstructures. *Model. Simul. Mater. Sci. Eng.* **2020**, *28*, 065002. [CrossRef]
23. Takaki, T.; Hirouchi, T.; Hisakuni, Y.; Yamanaka, A.; Tomita, Y. Multi-Phase-Field Model to Simulate Microstructure Evolutions during Dynamic Recrystallization. *Mater. Trans.* **2008**, *49*, 2559–2565. [CrossRef]
24. Takaki, T.; Tomita, Y. Static recrystallization simulations starting from predicted deformation microstructure by coupling multi-phase-field method and finite element method based on crystal plasticity. *Int. J. Mech. Sci.* **2010**, *52*, 320–328. [CrossRef]
25. Zhang, J.; Zheng, C.-W.; Li, D.-Z. A Multi-phase Field Model for Static Recrystallization of Hot Deformed Austenite in a C–Mn Steel. *Acta Metall. Sin. Engl. Lett.* **2018**, *31*, 208–215. [CrossRef]
26. Zhu, B.; Militzer, M. 3D phase field modelling of recrystallization in a low-carbon steel. *Model. Simul. Mater. Sci. Eng.* **2012**, *20*, 085011. [CrossRef]
27. Takaki, T.; Hisakuni, Y.; Hirouchi, T.; Yamanaka, A.; Tomita, Y. Multi-phase-field simulations for dynamic recrystallization. *Comput. Mater. Sci.* **2009**, *45*, 881–888. [CrossRef]
28. Takaki, T.; Yamanaka, A.; Tomita, Y. Phase-Field Modeling for Dynamic Recrystallization. In *From Creep Damage Mechanics to Homogenization Methods: A Liber Amicorum to Celebrate the Birthday of Nobutada Ohno*; Altenbach, H., Matsuda, T., Okumura, D., Eds.; Springer International Publishing: Cham, Switzerland, 2015; pp. 441–459.
29. Zhao, P.; Low, T.S.E.; Wang, Y.; Niezgoda, S.R. An integrated full-field model of concurrent plastic deformation and microstructure evolution: Application to 3D simulation of dynamic recrystallization in polycrystalline copper. *Int. J. Plast.* **2016**, *80*, 38–55. [CrossRef]
30. Zhao, P.; Wang, Y.; Niezgoda, S.R. Microstructural and micromechanical evolution during dynamic recrystallization. *Int. J. Plast.* **2018**, *100*, 52–68. [CrossRef]
31. Chen, L.; Chen, J.; Lebensohn, R.A.; Ji, Y.Z.; Heo, T.W.; Bhattacharyya, S.; Chang, K.; Mathaudhu, S.; Liu, Z.K.; Chen, L.Q. An integrated fast Fourier transform-based phase-field and crystal plasticity approach to model recrystallization of three dimensional polycrystals. *Comput. Methods Appl. Mech. Eng.* **2015**, *285*, 829–848. [CrossRef]
32. Creep polygonization and dynamic recrystallization. In *Creep of Crystals: High-Temperature Deformation Processes in Metals, Ceramics and Minerals*; Poirier, J.-P., Ed.; Cambridge University Press: Cambridge, UK, 1985; pp. 169–193.
33. Andrade, E.N.D.C. Creep of Metals and Recrystallization. *Nature* **1948**, *162*, 410. [CrossRef]
34. Stüwe, H.P.; Ortner, B. Recrystallization in Hot Working and Creep. *Met. Sci.* **1974**, *8*, 161–167. [CrossRef]
35. Spigarelli, S.; El Mehtedi, M. Creep as an extension of hot working: A unified approach to high temperature deformation of AZ31 alloy. *Mater. Sci. Eng. A* **2010**, *527*, 5708–5714. [CrossRef]
36. Estrin, Y.; Mecking, H. A unified phenomenological description of work hardening and creep based on one-parameter models. *Acta Metall.* **1984**, *32*, 57–70. [CrossRef]
37. Mecking, H.; Kocks, U.F. Kinetics of flow and strain-hardening. *Acta Metall.* **1981**, *29*, 1865–1875. [CrossRef]
38. Chu, S.N.G.; Li, J.C.M. Impression creep; a new creep test. *J. Mater. Sci.* **1977**, *12*, 2200–2208. [CrossRef]
39. Sastry, D.H. Impression creep technique—An overview. *Mater. Sci. Eng. A* **2005**, *409*, 67–75. [CrossRef]
40. Yang, Y.; Xiong, X.; Chen, J.; Peng, X.; Chen, D.; Pan, F. Research advances of magnesium and magnesium alloys worldwide in 2022. *J. Magnes. Alloys* **2023**, *11*, 2611–2654. [CrossRef]
41. Kim, H.-K.; Kim, W.-J. Creep behavior of AZ31 magnesium alloy in low temperature range between 423 K and 473 K. *J. Mater. Sci.* **2007**, *42*, 6171–6176. [CrossRef]
42. Luo, A.A. Recent magnesium alloy development for elevated temperature applications. *Int. Mater. Rev.* **2004**, *49*, 13–30. [CrossRef]
43. Kassner, M.E. Chapter 1—Fundamentals of Creep in Materials. In *Fundamentals of Creep in Metals and Alloys*, 3rd ed.; Kassner, M.E., Ed.; Butterworth-Heinemann: Boston, MA, USA, 2015; pp. 1–6.
44. Rezvani, A.; Ebrahimi, R. Mathematical Modeling of the Deformation Zone Under an Impression Creep Indenter Using Upper-Bound Theory. *J. Mater. Eng. Perform.* **2025**. [CrossRef]

45. Zhang, Y.; Yang, L.; Ge, C.; Pang, S.; Wang, X.; Zhang, Z.; Han, Z. Influence of Ca and Sr Addition on Impression Creep Behavior of Mg-4Al-RE Alloy. *J. Mater. Eng. Perform.* **2019**, *28*, 394–403. [CrossRef]
46. Kim, H.-K. The correlation between the impression and double shear creep of AZ31 magnesium alloy. *Mater. Sci. Eng. A* **2012**, *551*, 1–6. [CrossRef]
47. Naveena, J.; Kumar, G.; Mathew, M.D. Finite Element Analysis of Plastic Deformation During Impression Creep. *J. Mater. Eng. Perform.* **2015**, *24*, 1741–1753. [CrossRef]
48. Yang, F.; Li, J.C.M.; Shih, C.W. Computer simulation of impression creep using the hyperbolic sine stress law. *Mater. Sci. Eng. A* **1995**, *201*, 50–57. [CrossRef]
49. Nabariya, R.J.; Goyal, S.; Vasudevan, M.; Arivazhagan, N. Finite Element Analysis of Impression Creep. *Mater. Today Proc.* **2018**, *5 Pt 2*, 12320–12329. [CrossRef]
50. Teja, V.; Bedi, R.; Kumar, M. Finite Element Analysis of Impression Creep on P91. *IOP Conf. Ser. Mater. Sci. Eng.* **2022**, *1248*, 012023. [CrossRef]
51. Liu, X.; Li, L.-X.; He, F.-Y.; Zhou, J.; Zhu, B.-W.; Zhang, L.-Q. Simulation on dynamic recrystallization behavior of AZ31 magnesium alloy using cellular automaton method coupling Laasraoui–Jonas model. *Trans. Nonferrous Met. Soc. China* **2013**, *23*, 2692–2699. [CrossRef]
52. Chen, L.-Q. Phase-Field Models for Microstructure Evolution. *Annu. Rev. Mater. Res.* **2002**, *32*, 113–140. [CrossRef]
53. Moelans, N.; Blanpain, B.; Wollants, P. An introduction to phase-field modeling of microstructure evolution. *Calphad* **2008**, *32*, 268–294. [CrossRef]
54. Moelans, N.; Blanpain, B.; Wollants, P. Quantitative analysis of grain boundary properties in a generalized phase field model for grain growth in anisotropic systems. *Phys. Rev. B* **2008**, *78*, 024113. [CrossRef]
55. Moelans, N.; Blanpain, B.; Wollants, P. Quantitative Phase-Field Approach for Simulating Grain Growth in Anisotropic Systems with Arbitrary Inclination and Misorientation Dependence. *Phys. Rev. Lett.* **2008**, *101*, 025502. [CrossRef] [PubMed]
56. Humphreys, J.; Rohrer, G.S.; Rollett, A. Chapter 5—Mobility and Migration of Boundaries. In *Recrystallization and Related Annealing Phenomena*, 3rd ed.; Humphreys, J., Rohrer, G.S., Rollett, A., Eds.; Elsevier: Oxford, UK, 2017; pp. 145–197.
57. Moelans, N. A quantitative and thermodynamically consistent phase-field interpolation function for multi-phase systems. *Acta Mater.* **2011**, *59*, 1077–1086. [CrossRef]
58. Moelans, N.; Godfrey, A.; Zhang, Y.; Jensen, D.J. Phase-field simulation study of the migration of recrystallization boundaries. *Phys. Rev. B* **2013**, *88*, 054103. [CrossRef]
59. Allen, S.M.; Cahn, J.W. A microscopic theory for antiphase boundary motion and its application to antiphase domain coarsening. *Acta Metall.* **1979**, *27*, 1085–1095. [CrossRef]
60. Gruber, J.; Ma, N.; Wang, Y.; Rollett, A.D.; Rohrer, G.S. Sparse data structure and algorithm for the phase field method. *Model. Simul. Mater. Sci. Eng.* **2006**, *14*, 1189–1195. [CrossRef]
61. Vedantam, S.; Patnaik, B.S.V. Efficient numerical algorithm for multiphase field simulations. *Phys. Rev. E* **2006**, *73*, 016703. [CrossRef]
62. Turnbull, D. Theory of Grain Boundary Migration Rates. *JOM* **1951**, *3*, 661–665. [CrossRef]
63. Liu, Y.-X.; Lin, Y.C.; Li, H.-B.; Wen, D.-X.; Chen, X.-M.; Chen, M.-S. Study of dynamic recrystallization in a Ni-based superalloy by experiments and cellular automaton model. *Mater. Sci. Eng. A* **2015**, *626*, 432–440. [CrossRef]
64. Prosgolitis, C.G.; Lambrakos, S.G.; Zervaki, A.D. Phase-Field Modeling of Nugget Zone for a AZ31-Mg-Alloy Friction Stir Weld. *J. Mater. Eng. Perform.* **2018**, *27*, 5102–5113. [CrossRef]
65. Groh, S.; Marin, E.B.; Horstemeyer, M.F.; Bammann, D.J. Dislocation motion in magnesium: A study by molecular statics and molecular dynamics. *Model. Simul. Mater. Sci. Eng.* **2009**, *17*, 075009. [CrossRef]
66. Fan, D.; Chen, L.Q. Computer simulation of grain growth using a continuum field model. *Acta Mater.* **1997**, *45*, 611–622. [CrossRef]
67. Ning, Y.Q.; Wang, T.; Fu, M.W.; Li, M.Z.; Wang, L.; Zhao, C.D. Competition between work-hardening effect and dynamic-softening behavior for processing as-cast GH4720Li superalloys with original dendrite microstructure during moderate-speed hot compression. *Mater. Sci. Eng. A* **2015**, *642*, 187–193. [CrossRef]
68. Puchi-Cabrera, E.S.; Staia, M.H.; Guérin, J.D.; Lesage, J.; Dubar, M.; Chicot, D. An experimental analysis and modeling of the work-softening transient due to dynamic recrystallization. *Int. J. Plast.* **2014**, *54*, 113–131. [CrossRef]
69. Luo, F.; Peng, H.; Chen, H.; Xiao, X.; Xie, W.; Wang, H.; Yang, B. Dislocation substructure-controlled softening of Cu-20Ni-20Mn alloy. *Mater. Charact.* **2019**, *147*, 253–261. [CrossRef]
70. Frost, H.J.; Ashby, M.F. Deformation-Mechanism Maps: The Plasticity and Creep of Metals and Ceramics. Franklin Book Company, Incorporated: Elkins Park, PA, USA, 1982.
71. Honeycombe, R.W.K.; Pethen, R.W. Dynamic recrystallization. *J. Less Common Met.* **1972**, *28*, 201–212. [CrossRef]
72. Sakai, T.; Ohashi, M. Dislocation substructures developed during dynamic recrystallisation in polycrystalline nickel. *Mater. Sci. Technol.* **1990**, *6*, 1251–1257. [CrossRef]

73. Arsenlis, A.; Parks, D.M. Crystallographic aspects of geometrically-necessary and statistically-stored dislocation density. *Acta Mater.* **1999**, *47*, 1597–1611. [CrossRef]
74. Clemm, J.; Fisher, J.C. The influence of grain boundaries on the nucleation of secondary phases. *Acta Metall.* **1955**, *3*, 70–73. [CrossRef]
75. Wu, G.L.; Jensen, D.J. Orientations of recrystallization nuclei developed in columnar-grained Ni at triple junctions and a high-angle grain boundary. *Acta Mater.* **2007**, *55*, 4955–4964. [CrossRef]
76. Jokisaari, A.M.; Permann, C.; Thornton, K. A nucleation algorithm for the coupled conserved–nonconserved phase field model. *Comput. Mater. Sci.* **2016**, *112*, 128–138. [CrossRef]
77. Rezvani, A.; Ebrahimi, R.; Bagherpour, E. Static Recrystallization Simulation of Interstitial Free-Steel by Coupling Multi-Phase-Field and Crystal Plasticity Model Considering Dislocation Density Distribution. *Adv. Eng. Mater.* **2025**, 2500117. [CrossRef]
78. He, F.; Wu, C.; Shi, L. Phase-field simulation of dynamic recrystallization in friction stir weld nugget zone of dissimilar Al/Mg alloys. *J. Mater. Res. Technol.* **2023**, *27*, 2670–2683. [CrossRef]
79. Gladman, T. Creep Strength in Steel and High-Temperature Alloys. *Steel Times* **1972**, *200*, 910.
80. Mayes, P.; Hancock, P. Grain-boundary sliding and recrystallization of nimonic 108 during creep. *Met. Sci. J.* **1973**, *7*, 69–75. [CrossRef]
81. Mayes, F.; Hancock, P. Recrystallization of Nimonic 108 during Creep. *Met. Sci.* **1975**, *9*, 145–148. [CrossRef]
82. Koul, A.K.; Immarigeon, J.P.A. Dynamic recrystallization during creep in a 45 Pct Ni-35 pct Fe-20 pct Cr alloy system. *Metall. Trans. A* **1985**, *16*, 51–57. [CrossRef]
83. Gottstein, G. Dynamic recrystallization of Cu single crystals during tensile deformation in creep. *Met. Sci.* **1983**, *17*, 497–502. [CrossRef]
84. Larsen-Badse, J. Indentation creep of soft metals. In Proceedings of the Annual Meeting of AIME, Los Angeles, CA, USA, 19–23 February 1967.
85. Hyun, C.Y.; Kim, H.K. Creep deformation behaviour of AZ31 magnesium alloy over wide range of temperature and stress. *Mater. High Temp.* **2014**, *31*, 34–40. [CrossRef]
86. Korla, R.; Chokshi, A.H. A Constitutive Equation for Grain Boundary Sliding: An Experimental Approach. *Metall. Mater. Trans. A* **2014**, *45*, 698–708. [CrossRef]
87. Roodposhti, P.S.; Sarkar, A.; Murty, K.L. Microstructural development of high temperature deformed AZ31 magnesium alloys. *Mater. Sci. Eng. A* **2015**, *626*, 195–202. [CrossRef]
88. Essadiqi, E.; Liu, W.J.; Kao, V.; Yue, S.L.; Verma, R. Recrystallization in AZ31 Magnesium Alloy during Hot Deformation. *Mater. Sci. Forum* **2005**, *475–479*, 559–562. [CrossRef]